ROYAL SOCIETY
OF CHEMISTRY

PAPER

Check for updates

A green and sustainable approach using *Thuja occidentalis*-mediated Fe$_3$O$_4$ QDs decorated on rGO NSs for enhanced photocatalytic degradation of antibiotics

Ajay Potbhare,[†ab] Rohit Madankar,[†a] Shubham Tripathy,[a] Pavan Bhilkar,[a] Aniket Kahate,[a] Subhash Somkuwar,[c] Leonard Ng Wei Tat, [ID][d] Ahmed Abdala,*[e] Rameshwar Adhikari [ID] *[f] and Ratiram Chaudhary [ID] *[a]

Emerging pharmaceutical contaminants such as antibiotics, personal care products, and anti-inflammatory drugs have become major environmental concerns due to their persistence and toxicity. In this study, Fe$_3$O$_4$ quantum dots supported on reduced graphene oxide nanosheets (Fe$_3$O$_4$ QDs–rGO NSs) were successfully synthesized *via* a green hydrothermal route using *Thuja occidentalis* leaf extract as a natural reducing and capping agent. The resulting nanocomposites (NCs) exhibited a high surface area (168 m^2 g^{-1}) and mesoporous structure (average pore size ≈14 nm), favouring pollutant adsorption and charge separation. Under visible-light irradiation, the Fe$_3$O$_4$ QDs–rGO NSs demonstrated superior photocatalytic performance toward pharmaceutical contaminants, achieving degradation efficiencies of 94.5% for *ciprofloxacin* (CIP), 76.2% for *ibuprofen* (IBU), and 90.7% for *tetracycline* (THC) within 120 min at an optimum catalyst dose of 5 mg and neutral pH ≈ 7. The apparent first-order rate constants (*k*) were 0.024, 0.017, and 0.012 min^{-1} for CIP, IBU, and THC, respectively. The nanocomposite retained over 90% of its photocatalytic efficiency after five reuse cycles, confirming its excellent stability and recyclability. The enhanced activity is attributed to the synergistic interaction between Fe$_3$O$_4$ QDs and rGO, which promotes efficient charge carrier separation and radical generation. These results highlight the potential of bioinspired Fe$_3$O$_4$ QDs–rGO NSs as an efficient, sustainable photocatalyst for wastewater remediation applications.

1. Introduction

Human society faces various environmental challenges due to the growing global population and urbanization. One of the biggest challenges is water pollution, which arises from pharmaceutical waste, laboratory chemicals, agricultural activities, microorganisms, oil spills, sewage, wastewater, radioactive waste, plastic waste, mining activities, industrial waste and so forth. In particular, agricultural wastewater contains a variety of

harmful organic and inorganic pollutants, such as heavy metal ions, dyes, pesticides, antibiotics, and fertilizers.[1–5] These contaminants significantly deteriorate water quality and pose significant threats to the environment, human health, aquatic life, flora and fauna. To tackle this challenge, researchers worldwide are developing innovative techniques and advanced multifunctional materials to eradicate such hazardous pollutants.[6,7] Among the various strategies, nature-inspired fabrication is an emerging technique as it is sustainable, economical, eco-friendly, green, non-hazardous, nontoxic, and biocompatible. Bioinspired nanotechnology is a breakthrough in the field of nanoscience and bionanotechnology. Indeed, it is an alternative to traditional nanotechnology, leading to a linkage between biotechnology, microbiology, and nanotechnology. The biosynthesis of nanocomposites (NCs) involves microorganisms, algae, enzymes, yeasts, biowaste, and plant extracts (*i.e.*, flowers, leaves, fruits, peels, stems, seeds, and roots). Bioinspired carbon-based materials are highly promising emerging materials in the field of bionanoscience.[8–10] Carbon-based nanomaterials (NMs) such as graphene oxide (GO), activated carbon, and carbon composites have garnered

[a]Post Graduate Department of Chemistry, Seth Kesarimal Porwal College, RTM Nagpur University, Nagpur, Kamptee, 441001, India. E-mail: chaudhary_rati@yahoo.com

[b]Department of Chemistry, Smt. Panchashila Arts, Science, and Commerce Womens College, Hardoli, Bhandara-441915, India

[c]Department of Botany, Dr Ambedkar College, Deekshabhoomi, Nagpur-440010, India

[d]School of Materials Science and Engineering, Nanyang Technological University, 50 Nanyang Avenue, 639798, Singapore

[e]College of Science and Engineering, Hamad Bin Khalifa University, POB 34111, Doha, Qatar. E-mail: ahabdalla@hbku.edu.qa

[f]Department of Chemistry, Tribhuvan University, Kathmandu, 44600, Nepal. E-mail: nepalpolymer@yahoo.com

† First authorship: Ajay K. Potbhare and Rohit S. Madankar.

considerable interest due to their cost-effectiveness, wide availability, and potential to enhance the performance of nanoparticles (NPs). In particular, graphene oxide has been extensively employed over the past two decades to synthesize graphene-coated NPs. Its unique two-dimensional structure, composed of sp²-hybridized carbon atoms confers exceptional chemical and optical properties. Moreover, graphene-based materials possess high surface area, excellent adsorption capacity, thermal stability, and superior conductivity for diverse applications.[11–15]

Although graphene-based metal oxide NCs are excellent materials for the removal of organic pollutants due to their high separation ability and catalytic activity,[16,17] photocatalysis is a superior methodology for degrading organic pollutants, antibiotics, pharmaceutical drugs, and phenolic compounds.[18–20] Thus, the excellent photocatalytic efficiency of graphene-based metal oxide NCs might be due to their unique surface area and wide bandgap, which facilitate the transfer of the photo-excited electron from the conduction band to the valence band, ultimately exploiting the enhanced photochemical reaction.[21–23] The marvellous properties of graphene-based NCs make them an excellent choice for the photodegradation of some antibiotics. Decorating magnetic NPs on the surface of reduced graphene oxide (rGO) significantly enhances their separation efficiency. The magnetic responsiveness facilitates the easy recovery of NCs after treatment. This structure also imparts vigorous catalytic activity for the removal of harmful contaminants from aqueous solutions. The integration of graphene contributes to a synergistic interaction between rGO and Fe$_3$O$_4$ NPs, which plays a crucial role in boosting the overall performance of the NCs. This synergy is a key factor behind the improved effectiveness of Fe$_3$O$_4$ QDs–rGO NSs in environmental remediation applications.[24–28]

Furthermore, the inherent magnetic properties of Fe$_3$O$_4$ QDs enable easy recovery of the NCs from treated water using an external magnetic field, allowing for recyclability and minimizing secondary pollution. This dual functionality of high photocatalytic activity and magnetic separability makes Fe$_3$O$_4$ QDs–rGO NSs ideal for practical environmental applications. The current research not only advances our understanding of plant-mediated NMs synthesis but also demonstrates a sustainable and effective approach for the removal of hazardous pharmaceutical pollutants from aquatic environments.[29–33]

In the present study, we report the novel, green synthesis of Fe$_3$O$_4$ QDs–rGO NSs using a *Thuja occidentalis* leaf extract *via* a one-step hydrothermal method. This eco-friendly strategy leverages the natural reducing potential of phytochemicals to synthesize Fe$_3$O$_4$ QDs under mild conditions, avoiding the use of harsh chemicals or external stabilizers. The resulting Fe$_3$O$_4$ QDs–rGO NSs were systematically characterized and evaluated for their photocatalytic performance against pharmaceutical contaminants, including common antibiotics and drug residues. The synergistic interaction between Fe$_3$O$_4$ QDs and rGO NSs enhances charge carrier separation, suppresses recombination, and extends visible-light absorption, key factors that drive superior photocatalytic efficiency. The *Thuja occidentalis*

leaf extract acted as a biosurfactant and a capping agent, effectively reducing GO to rGO and iron ions to iron oxide QDs. Additionally, the extract was crucial in preventing Fe$_3$O$_4$ QDs agglomeration and enhancing the structural, optical, electrical, and morphological properties of the Fe$_3$O$_4$ QDs. The resulting nature-inspired Fe$_3$O$_4$ QDs–rGO NSs were evaluated for photocatalytic degradation of pharmaceutical contaminants. Remarkably, the Fe$_3$O$_4$ QDs–rGO NSs demonstrated excellent photocatalytic performance against antibiotics. These findings emphasize that plant-mediated Fe$_3$O$_4$ QDs–rGO NSs are effective for wastewater treatment and environmental remediation.

2. Experimental

2.1. Materials

Ferric chloride (FeCl$_3$·6H$_2$O) and ferrous sulfate (FeSO$_4$·7H$_2$O) (99.1% purity) were procured from Loba Chemie Pvt. Ltd Mumbai, India. Graphite powder was obtained from Platonic Nanotech Private Limited, Mohanpur, India. Ammonia solution, acetone, and ethanol were also obtained from the Fine Chem Industry research laboratory in Mumbai, India.

2.2. Preparation of plant extract

The *Thuja occidentalis* leaves were collected from the college garden. After being collected, the leaves of *Thuja occidentalis* underwent a cleansing process using distilled water, and subsequently, the leaves were dried for a few days. The dried leaves were ground to a fine powder using a grinder/mixer. Then, 20 g of fine leaves powder of *Thuja occidentalis* was taken in 100 mL double-distilled water and heated for 1.5 h at 60–70 °C with constant stirring until the volume of the solution was reduced to half. Finally, the solution was filtered using a Buchner flask and a suction pump in hot conditions to obtain the plant extract.[34]

2.3. Synthesis of graphene oxide (GO)

GO was synthesized by oxidation of graphite flakes using the improved Hummers' method.[35] In a typical synthesis, 3 g of graphite flakes were added to a flask containing 80 mL of conc. H$_2$SO$_4$ and kept below 15 °C by placing the flask in an ice bath. The graphite suspension in H$_2$SO$_4$ was stirred for 30 minutes to form a homogeneous suspension. Subsequently, KMnO$_4$ (9 g) was added to the suspension, and the temperature was raised to 50 °C with continual stirring for 1 h. Then, 20 mL of H$_2$O and 30 mL of H$_2$O$_2$ (30%) solution were added to the suspension. This step is associated with a color change from yellow to brown. The obtained brown color precipitate was filtered and washed with 1 : 10 HCl and H$_2$O until metal (Mn) ions were removed. Lastly, GO was dried in an oven at 70 °C for 12 h.[36]

2.4. *Thuja occidentalis* leaf extract-mediated synthesis of Fe$_3$O$_4$ QDs–rGO NSs

For the phytosynthesis of Fe$_3$O$_4$ QDs–rGO NSs *via* a hydrothermal method, 40 mg of GO was dispersed in 60 mL of deionized water and ultrasonicated for 1 h to achieve exfoliated graphene oxide (EGO). Then, FeCl$_3$ (2 mM) and FeSO$_4$·7H$_2$O (2 :
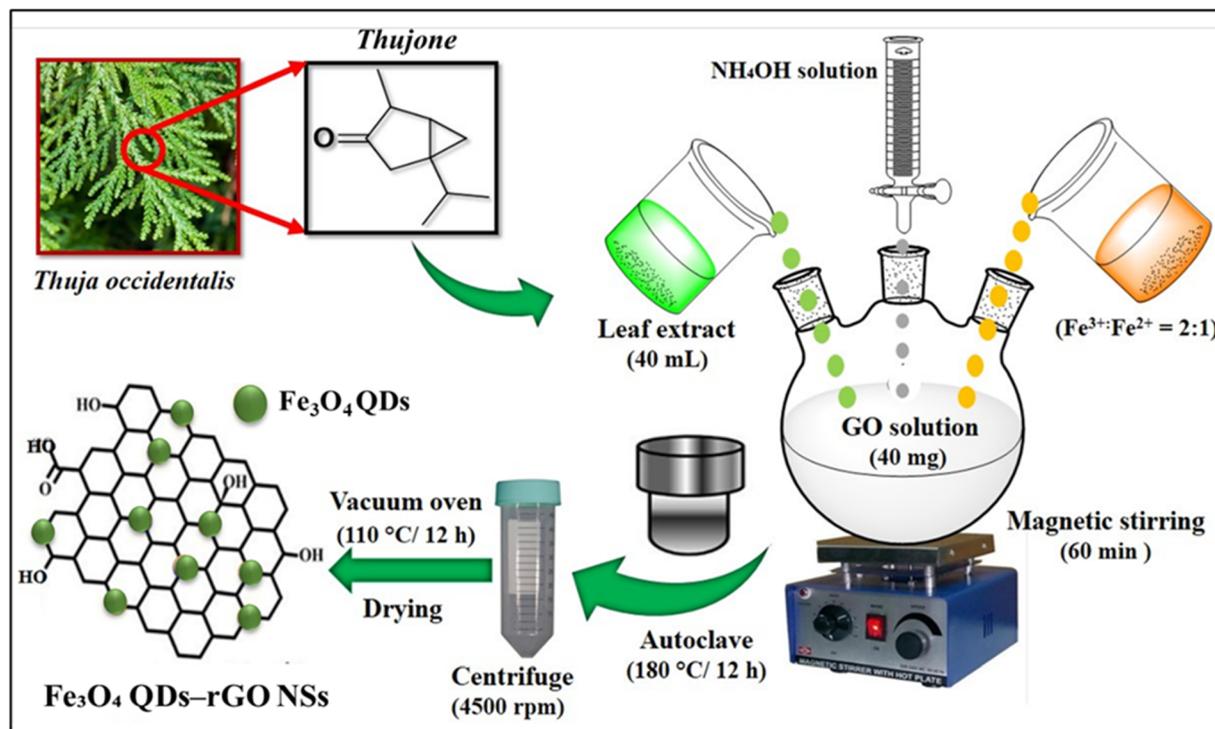
Fig. 1 *Thuja occidentalis* leaf extract-mediated biosynthesis of Fe_3O_4 QDs on rGO NSs.

1) (1 mM) were added to the exfoliated graphene oxide solution. The reaction mixture was stirred for 30 min to form a uniform suspension, and then about 40 mL of *Thuja occidentalis* leaf extract was added, followed by stirring for 60 min. The pH of the suspension was adjusted to 10 by adding ammonium solution. Subsequently, the obtained suspension was transferred to a Teflon-lined autoclave for hydrothermal treatment at 180 °C for 12 h.[37] Then, the precipitate was centrifuged at 4500 rpm and washed thrice with distilled water and absolute ethanol to remove the *Thuja occidentalis* leaf extract biomass, and dried in a vacuum oven at 110 °C overnight. The obtained brown-colored product was designated as Fe_3O_4 QDs–rGO NSs (Fig. 1) and characterized by standard spectroscopic techniques to determine its structure, size, shape, and morphology.

2.5. Characterization of GO and Fe_3O_4 QDs–rGO NSs

X-ray diffraction (XRD) was performed on a Bruker (AXS D8 Advance) diffractometer using Cu Kα radiation at $\lambda = 0.154$ nm, while Fourier transform infrared (FTIR) spectra were recorded in the range of 400–4000 cm^{-1} using a Bruker (IFS 66v) spectrophotometer. Qualitative elemental analysis was performed using energy dispersive spectroscopy (EDS; Oxford Instruments), and an X-ray photoelectron spectroscopy (ESCALAB 250 XPS, Al Ka (150 W)) system was used for chemical state identification. UV-visible diffuse reflectance spectra were recorded using a spectrophotometer (UV-DRS; Cary-100UV), while Raman spectroscopy was performed using a JY Horiba (HR-800) spectrophotometer. Transmission electron microscopy (TEM: JEOL-JEM 100SX) was used to study the surface morphology. A

micromeritic ASAP 2010 BET analyser was used for surface area and porosity determination.

2.6. Photocatalytic activity measurement

The photocatalytic activity of the Fe_3O_4 QDs–rGO NSs for the degradation of CIP, IBU, and THC was studied under visible-light irradiation. The photocatalytic reactor was equipped with a cylindrical tungsten lamp as a visible-light source. The photocatalytic experiments were conducted under visible-light irradiation using a 400-W tungsten halogen lamp (Philips, India) positioned 15 cm above the reactor. The lamp emitted light in the wavelength range of 400–750 nm with an integrated intensity of approximately 120 mW cm^{-2}, measured at the solution surface using a digital lux meter (LX-1010B). A water-circulated quartz cooling jacket surrounded the lamp to prevent thermal effects, maintaining the suspension temperature at 25 ± 2 °C throughout the experiment. The solution was magnetically stirred continuously to ensure uniform irradiation and prevent catalyst sedimentation. Concentrations of 5, 10, 15, 20 and 25 ppm of CIP, IBU, and THC were used for the experiments. Similarly, the photocatalyst dosage (5, 10, 15, and 20 mg) was varied for the photodegradation study. Subsequently, Fe_3O_4 QDs–rGO NSs (10 mg) were dispersed in 50 mL of 5, 10, 15, 20 and 25 ppm aqueous dye solution (pH = 7) at 25 ± 2 °C. Prior to light illumination, the suspension was stirred in the dark for 60 min to reach adsorption–desorption equilibrium. Subsequently, the 50 mL suspension was exposed to visible light in the photocatalytic reactor. Aliquots of the solution (5 mL) were removed from the reactor at 15 min intervals and

centrifuged to eradicate the corresponding photocatalyst, then the absorption was measured using a UV-vis spectrophotometer (ELICO Double Beam SL-210 UV-vis spectrophotometer), and the dye degradation percentage was calculated from the concentration of the initial dye (10 ppm) (C_0) and the dye concentration at time 't' of the visible-light exposure (C_t) as follows:

$$\text{Degradation efficiency (\%)} = \{(C_0 - C_t)/C_0\} \times 100 \quad (1)$$

However, the kinetic study of the Fe_3O_4 QDs–rGO photocatalyst using the Langmuir–Hinshelwood model for the analysis of the order of reaction, the apparent pseudo-first-order rate constant (k, mol m^{-3} h^{-1}) of the degradation reaction catalysed using the Fe_3O_4 QDs–rGO photocatalyst is determined by plotting C_t/C_0 versus irradiation time (t) using the following equation:

$$-\ln(C_t/C_0) = kt$$

2.7. Recyclability

The recyclability of the Fe_3O_4 QDs–rGO NSs was determined after complete deterioration of the corresponding dye; the NSs were recovered by filtration, washed multiple times, dried at

110 °C, and reused again. This was repeated for five cycles, and the Fe_3O_4 QDs–rGO NSs reusability results in terms of % degradation in each cycle are presented in Fig. 13. The results indicated no loss of photocatalytic efficiency up to the first 2 cycles, and a slight decrease in efficiency was observed during cycles 3, 4 and 5.

3. Results and discussion

3.1. Characterization of Fe_3O_4 QDs–rGO NSs

The XRD pattern of the nature-inspired Fe_3O_4 QDs–rGO NSs is depicted in Fig. 2(a). The diffraction peaks observed at 2θ = 30.30°, 35.60°, 43.35°, 53.84°, 57.32°, and 62.90° correspond to the (220), (311), (400), (422), (511), and (440) crystallographic planes, respectively. These peaks are in excellent agreement with the standard diffraction pattern of magnetite (Fe_3O_4) phase, as indexed by JCPDS card no. 26-1136, confirming the formation of pure cubic spinel γ-Fe_3O_4 structure with space group symmetry Fd-3m, no. 227. The presence of a strong and sharp (311) peak at 35.60° further affirms the high crystallinity of the synthesized NPs. The average crystallite size of the Fe_3O_4 QDs–rGO NSs, calculated using the Debye–Scherrer equation, was found to be approximately 14.02 nm, suggesting nanoscale crystallinity. Importantly, the XRD pattern of the composite material does not show the typical broad peaks of amorphous
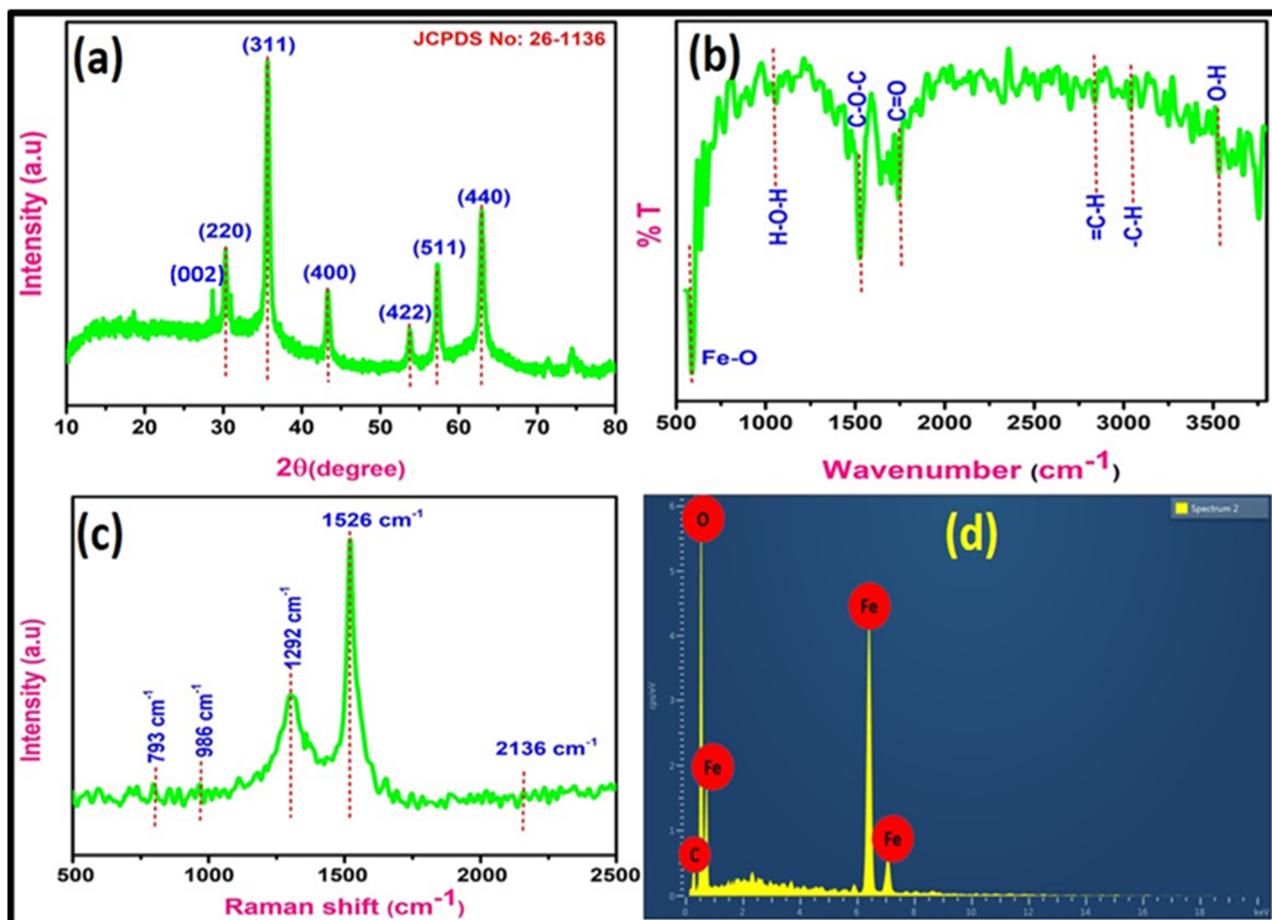

Fig. 2 (a) XRD pattern, (b) FTIR spectrum, (c) Raman spectrum, and (d) EDS of Fe_3O_4 QDs–rGO NSs.

carbon or pristine graphene oxide (GO), which generally appear at around $2\theta \approx 10°$ and $2\theta \approx 26°$, corresponding to the (001) and (002) planes, respectively. The absence or weakening of these peaks can be attributed to the reduction of GO to rGO during the synthesis process, and the effective exfoliation and dispersion of rGO NSs within the Ns matrix. Moreover, the strong diffraction peaks of Fe_3O_4 may mask the relatively weak signals of rGO, and typically appear as a broad hump near 28–29° corresponding to the (002) plane for disordered graphitic structures. The intimate interaction between the Fe_3O_4 QDs and the rGO NSs is implied from the homogeneous XRD profile, suggesting that rGO acts as a stabilizing support and provides an anchoring platform for the nucleation and uniform distribution of Fe_3O_4 QDs. This hybrid structure is advantageous for applications requiring high conductivity, surface area, and magnetic responsiveness, such as environmental remediation and catalysis.[38]

The Fourier transform infrared (FTIR) spectrum of the Fe_3O_4–rGO NCs is illustrated in Fig. 2(b), revealing multiple characteristic absorption bands that confirm the formation and functional integration of both Fe_3O_4 QDs and rGO NSs. The distinct band observed around 580 cm^{-1} is assigned to the Fe–O stretching vibration, which is a typical fingerprint of the magnetite (Fe_3O_4) phase, indicating the presence of metal–oxygen bonds within the spinel structure. In the higher wavenumber region, several functional groups related to rGO are identified. The absorption bands observed near 1050–1150 cm^{-1} are attributed to C–O–C bending vibrations, which indicate the presence of residual epoxy or ether groups on the graphene framework. A prominent peak around 1720 cm^{-1} corresponds to the C=O stretching vibration of carbonyl or carboxylic groups, which are commonly present on partially reduced graphene oxide surfaces. These oxygenated groups arise from the incomplete reduction of graphene oxide and provide active sites for the anchoring of Fe_3O_4 QDs. Additionally, the bands in the region of 2850–2950 cm^{-1} can be ascribed to aliphatic –C–H stretching vibrations, whereas the broad peak centred near 3420 cm^{-1} is attributed to –OH stretching, originating from surface-adsorbed water molecules or hydroxyl groups on the rGO sheets and Fe_3O_4 surface. The presence of O–H stretching also confirms the hydrophilic nature of the composite and its good dispersibility in aqueous environments. The coexistence of both Fe–O bonds and various oxygen-containing functional groups of rGO NSs in the spectrum indicates the successful formation of the Fe_3O_4 QDs–rGO NSs. Moreover, the interaction between Fe_3O_4 NPs and rGO sheets can be inferred from the shift or broadening of some characteristic peaks, which suggests the formation of chemical or electrostatic interactions at the interface. The FTIR results support the structural and chemical integration of magnetic QDs with the rGO NSs, which is critical for enhancing the NC's properties for environmental and catalytic applications.[39]

Furthermore, the intimate interaction between Fe_3O_4 QDs and rGO NSs arises from both chemical and electrostatic bonding mechanisms established during the hydrothermal synthesis. The oxygen-containing functional groups (–OH, –COOH, and –C=O) present on partially reduced graphene oxide

act as nucleation and anchoring sites for Fe^{2+} and Fe^{3+} ions, facilitating the formation of Fe–O–C linkages. These chemical bonds, supported by FTIR and XPS observations, confirm the successful coupling of Fe_3O_4 with the rGO matrix. In addition, electrostatic attraction between positively charged Fe ions and negatively charged rGO sheets ensures uniform QD dispersion. This intimate Fe–O–C interface enables effective electron transfer across the Fe_3O_4–rGO junction, thereby suppressing charge recombination and enhancing the photocatalytic efficiency of the NCs.

Further, the Raman spectrum of the phytosynthesized Fe_3O_4 QDs–rGO NSs was studied to find the structure (Fig. 2(c)). The spectrum of Fe_3O_4 QDs–rGO NSs exhibits two-phonon scattering peaks at 793 cm^{-1} for the Ag mode and 986 cm^{-1} for the Bg mode. The Raman spectrum for the Fe_3O_4 QDs–rGO shows two bands located at 1292 and 1526 cm^{-1}, allocated to D and G bands, respectively, and the broad peak at 2136 cm^{-1} resembles the 2D peak of rGO. Of these, the presence of D and G bands is due to chaotic atomic interaction triggered by sp^3-hybridized carbon atoms and plane vibration of sp^2-hybridized carbon atoms in rGO NSs. Hence, the Raman spectrum confirmed the formation of Fe_3O_4 QDs–rGO NSs using hydrothermal methods.[40]

Moreover, the elemental composition and purity of the synthesized NCs were analysed by EDX spectroscopy, as shown in Fig. 2(d). The elemental peaks of Fe, O, and C confirmed the presence of graphene and Fe_3O_4 QDs in the biosynthesized material; hence, it indicates the presence of pure Fe_3O_4 phase. However, no traces of additional elements were observed; thus, it confirms the purity of the Fe_3O_4 QDs–rGO NSs. Additionally, the results are in good agreement with the XRD configurations. Elemental analysis indicates the presence of Fe (66.29%), C (5.36%) and O (28.35%). Hence, the study confirmed the purity of the Fe_3O_4 QDs–rGO NSs.[41]

Further, the N_2 adsorption/desorption isotherm (Fig. 3(a)) exposes adsorption on mesoporous materials via multilayer adsorption followed by capillary condensation, consistent with typical features of type IV isotherms, including a hysteresis loop, connected with capillary condensation in mesopores and restrictive uptake over a high P/P_0 range.[42] The measured BET surface area and average pore size of the Fe_3O_4 QDs–rGO NSs are 168 $m^2 g^{-1}$ and 14.2 nm, respectively. The pore size of the NCs revealed its mesoporous nature, while the relatively high specific surface area is due to its nanoscale size.

The thermogram for the Fe_3O_4 QDs–rGO NSs (Fig. 3(b)) depicts three stages of thermal decomposition. The first stage of thermal decomposition occurs in the 50–120 °C range, with mass loss of 4% assigned to the loss of water molecules. During the second step of degradation (120–400 °C), 12% mass loss was observed with a maximum degradation rate at 320 °C, maybe due to functional groups on graphene oxide. Similarly, lower mass loss was observed (~5%) in the third stage (400–900 °C), which was attributed to the degradation of carbon moieties. Further, no weight loss was observed above 900 °C, indicating the formation of a thermally stable ferrous oxide material.[43]
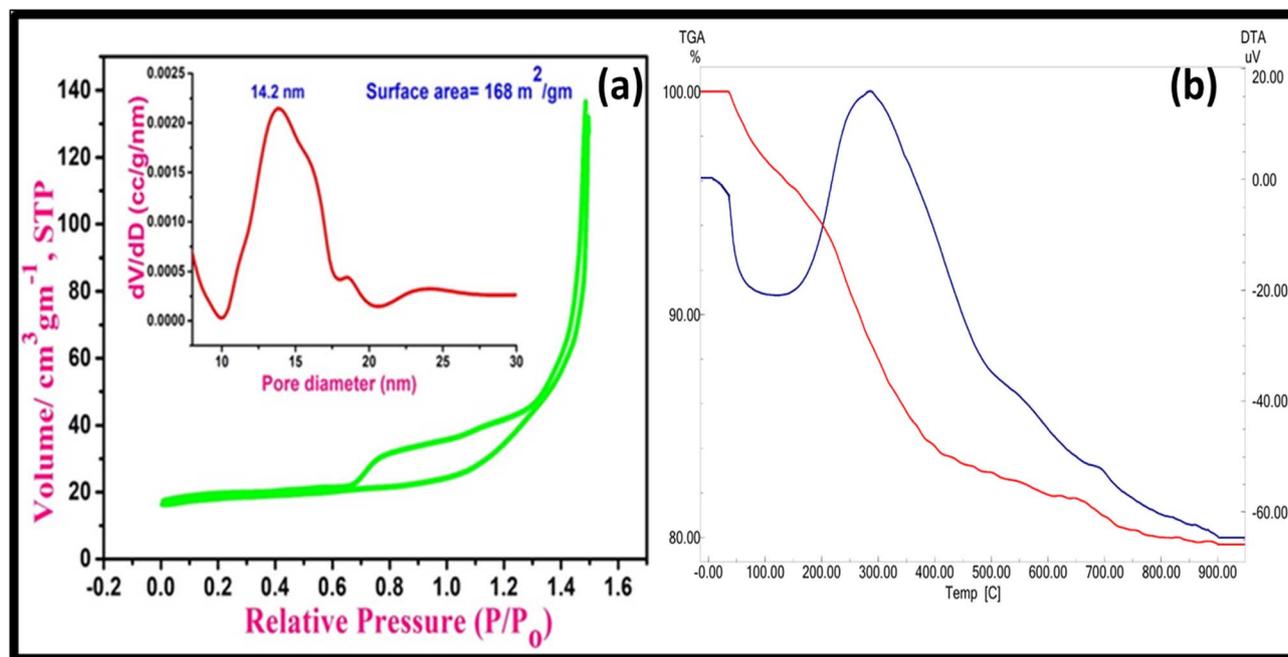
Fig. 3 (a) Nitrogen adsorption and desorption isotherm plot and (b) TG/DTA of Fe_3O_4 QDs–rGO NSs.

Next, the chemical configuration, oxidation states, and structure of the Fe_3O_4 QDs–rGO NSs were analysed using XPS [Fig. 4(a–d)].

The XPS survey spectrum of Fe_3O_4 QDs–rGO NSs confirmed the presence of iron (Fe), oxygen (O), and carbon (C) (Fig. 4(a)).

Moreover, the Fe-2p high-resolution spectrum (Fig. 4(b)) shows two peaks at binding energy of 709.15 eV and 724.83 eV, corresponding to the $Fe-2p_{3/2}$ and $Fe-2p_{1/2}$, respectively, suggesting the presence of ferric (+3), and ferrous (+2) oxide. The O-1s high-resolution spectrum (Fig. 4(c)) exhibits two peaks at 529.48 eV
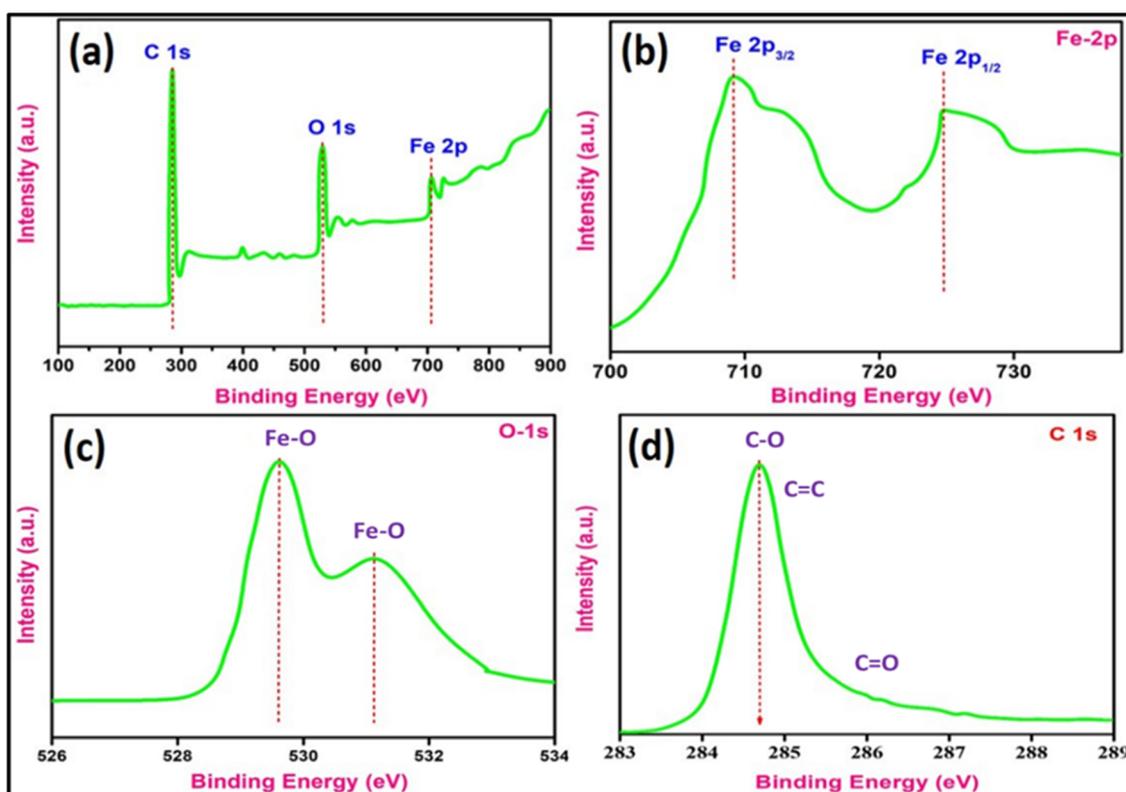

Fig. 4 XPS study of Fe_3O_4 QDs/rGO NSs: (a) survey spectrum, (b) Fe 2p, (c) O 1s, and (d) C 1s.

and 531.21 eV, confirming the existence of O^{2-}. The high-resolution spectrum of carbon (Fig. 4(d)) reveals a peak at 284.8 eV, which might have come from the unintentional presence of hydrocarbon in the XPS instrument.[44]

3.2. Morphological exploration of Fe₃O₄ QDs/rGO NSs

The morphology, including the shape and particle size of the phytosynthesized Fe₃O₄ QDs–rGO NSs was analysed by SEM and TEM. The SEM images in Fig. 5(a–d) reveal a nearly homogenised and dense distribution of Fe₃O₄ QDs. These QDs were anchored on the surface of the rGO NSs (Fig. 5(a–d)).[45]

Fig. 5 shows the surface morphology and structural organization. The low-magnification SEM image in Fig. 5 reveals the overall composite structure, where Fe₃O₄ QDs are nearly uniformly anchored/decorated on the wrinkled NSs of rGO. The rGO NSs are clearly visible as thin, flaky structures, offering a large surface area for NPs attachment and preventing agglomeration. In Fig. 5(b), the Fe₃O₄ QDs appear as roughly spherical granules with an average particle size of approximately 91.5–99.5 nm. Each spherical granule is constituted of a couple of QDs. The NPs are distributed across the rGO layers, suggesting strong interactions between the Fe₃O₄ QDs and the rGO NSs. Fig. 5(c) further highlights the intimate contact between the Fe₃O₄ QDs and the rGO NSs, with the red-circled region emphasizing the embedded nature of the NPs within the graphene surface. This configuration facilitates enhanced interfacial bonding, which is critical for improving the electrical conductivity and magnetic properties of the composite. In Fig. 5(d), the NPs maintain their spherical morphology with a particle size of approximately 82 nm, and appear to be nearly uniformly dispersed without significant agglomeration. The rGO NSs serve not only as a support but also as a stabilizing platform that allows for the even distribution and structural integrity of the composite.

Moreover, Fig. 6(a–f) the present results of the HR-TEM analysis of the Fe₃O₄ QDs–rGO NSs, illustrating their detailed morphological and structural characteristics. In Fig. 6(a), Fe₃O₄ QDs are seen densely distributed over the layered rGO NSs, confirming successful anchoring and dispersion. The rGO layers serve as a supportive matrix, effectively preventing NPs agglomeration. Fig. 6(b) highlights a clustered aggregation of Fe₃O₄ QDs, while Fig. 6(c and d) further magnifies these regions, showing dense particle networks embedded in the rGO framework. High-magnification Fig. 6(c) shows Fe₃O₄ particle sizes ranging between 5.2 nm to 8.6 nm, confirming their nanocrystalline nature.

The Fe₃O₄ QDs–rGO NSs display an average particle size of 7 ± 2 nm, indicating a well-dispersed decoration of Fe₃O₄ QDs on the rGO NSs, and further supporting particle size reduction.[46] In Fig. 6(e), the observed lattice fringe with a d-spacing of 0.18 nm corresponds to the (220) plane of Fe₃O₄, consistent with the XRD findings, confirming the crystalline quality of the NPs. Further, the SAED pattern in Fig. 6(f) shows sharp and well-

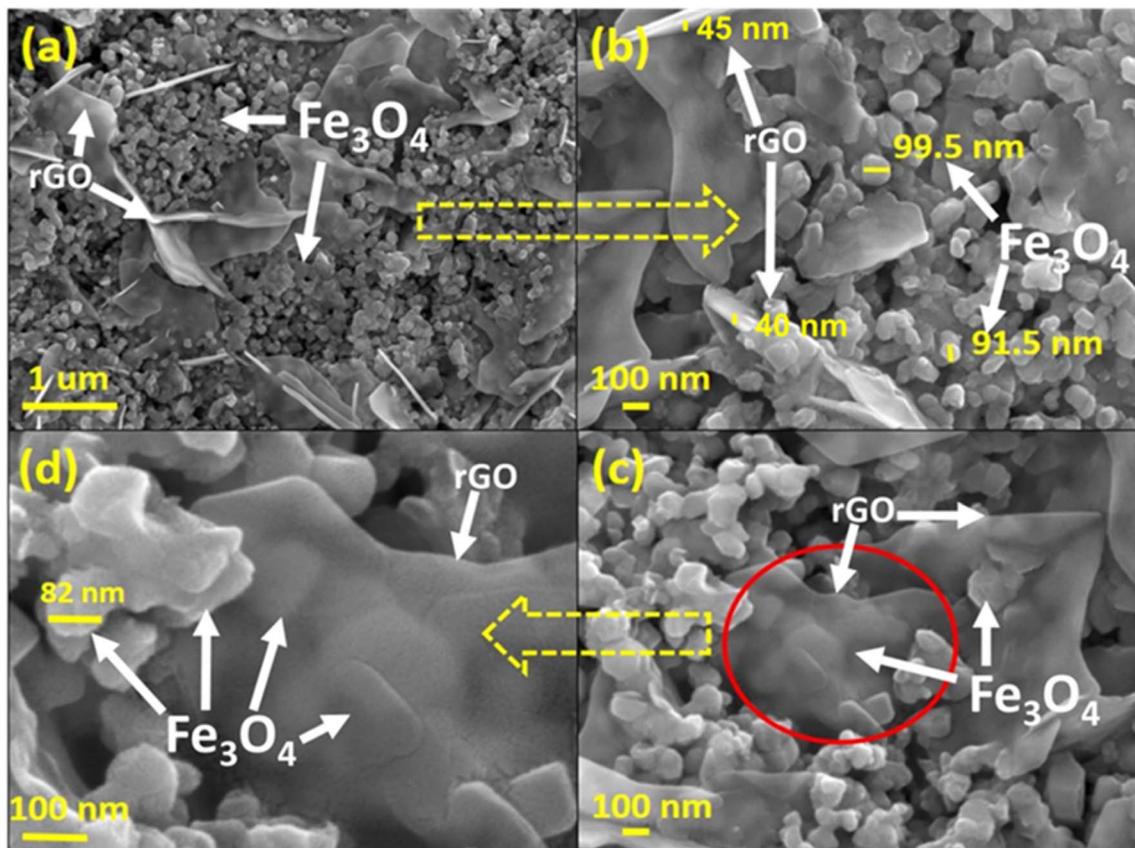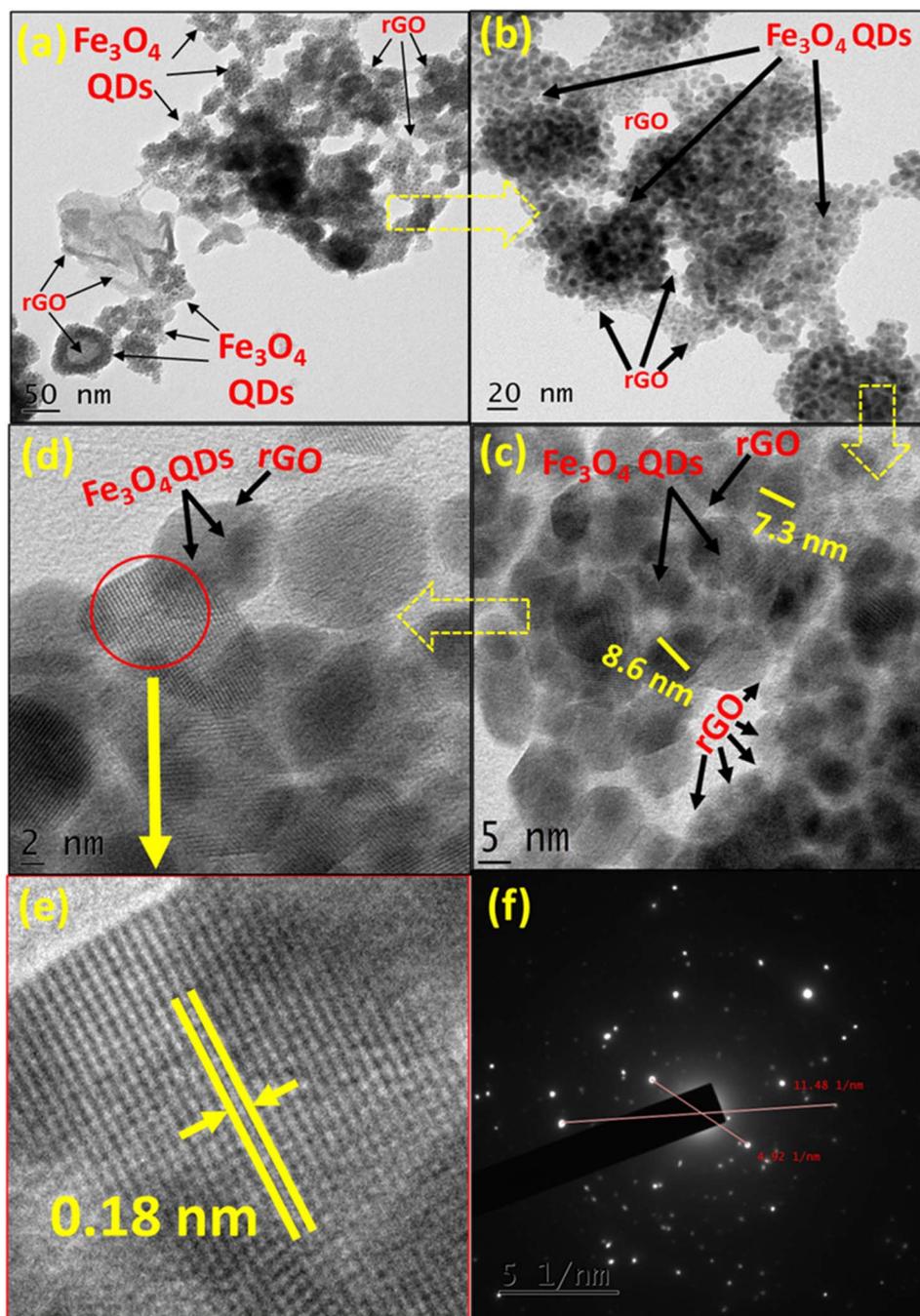Fig. 5   (a–d) SEM images of different magnifications of Fe₃O₄ QDs on rGO NSs.

Fig. 6 (a–e) TEM images of different magnifications of Fe_3O_4 QDs on rGO NSs and (f) electron diffraction pattern of the material.

defined diffraction rings indexed to Fe_3O_4, with prominent reflections at 11.48 and 4.32 1/nm, verifying the polycrystalline nature of the Fe_3O_4 QDs–rGO NSs.[47]

These TEM observations are strongly supported by the SEM images (Fig. 5), which further revealed the surface morphology and macro-structure of the Fe_3O_4 QDs–rGO NSs. In Fig. 6(a), rGO sheets appeared as thin wrinkled layers over which spherical Fe_3O_4 QDs–rGO are uniformly distributed. Meanwhile, Fig. 5(b–d) show close-up views of these distributions, where particle sizes are found to be in the range of 82–99.5 nm, with

Fe_3O_4 NPs embedded within and overlaid on rGO layers. Fig. 6(d) confirm strong interaction between the Fe_3O_4 QDs and rGO NSs. While SEM presents slightly larger particle dimensions due to possible agglomeration and surface accumulation, TEM confirms the intrinsic nanoscale dimensions and crystalline nature of the individual Fe_3O_4 QDs. Together, the complementary SEM and TEM analyses confirm the successful synthesis of Fe_3O_4 QDs–rGO NSs, exhibiting well-dispersed nanocrystals with strong interfacial contact.

3.3. Photocatalytic performance of Fe₃O₄ QDs/rGO NSs

The photocatalytic degradation performance of the Fe_3O_4 QDs–rGO NSs was evaluated against three pharmaceutical contaminants: CIP, IBU, and THC. The time-dependent UV-vis absorption spectra and corresponding degradation kinetics (C_t/C_0 vs.

time) for different initial concentrations (10–40 ppm) were systematically analysed. The UV-visible spectra in Fig. 7 show a steady decrease in the absorbance peaks over time, particularly at ~275 nm and ~325 nm, indicating progressive degradation of CIP. The degradation kinetics shown in Fig. 7(b) illustrate that lower concentrations degrade more rapidly, with
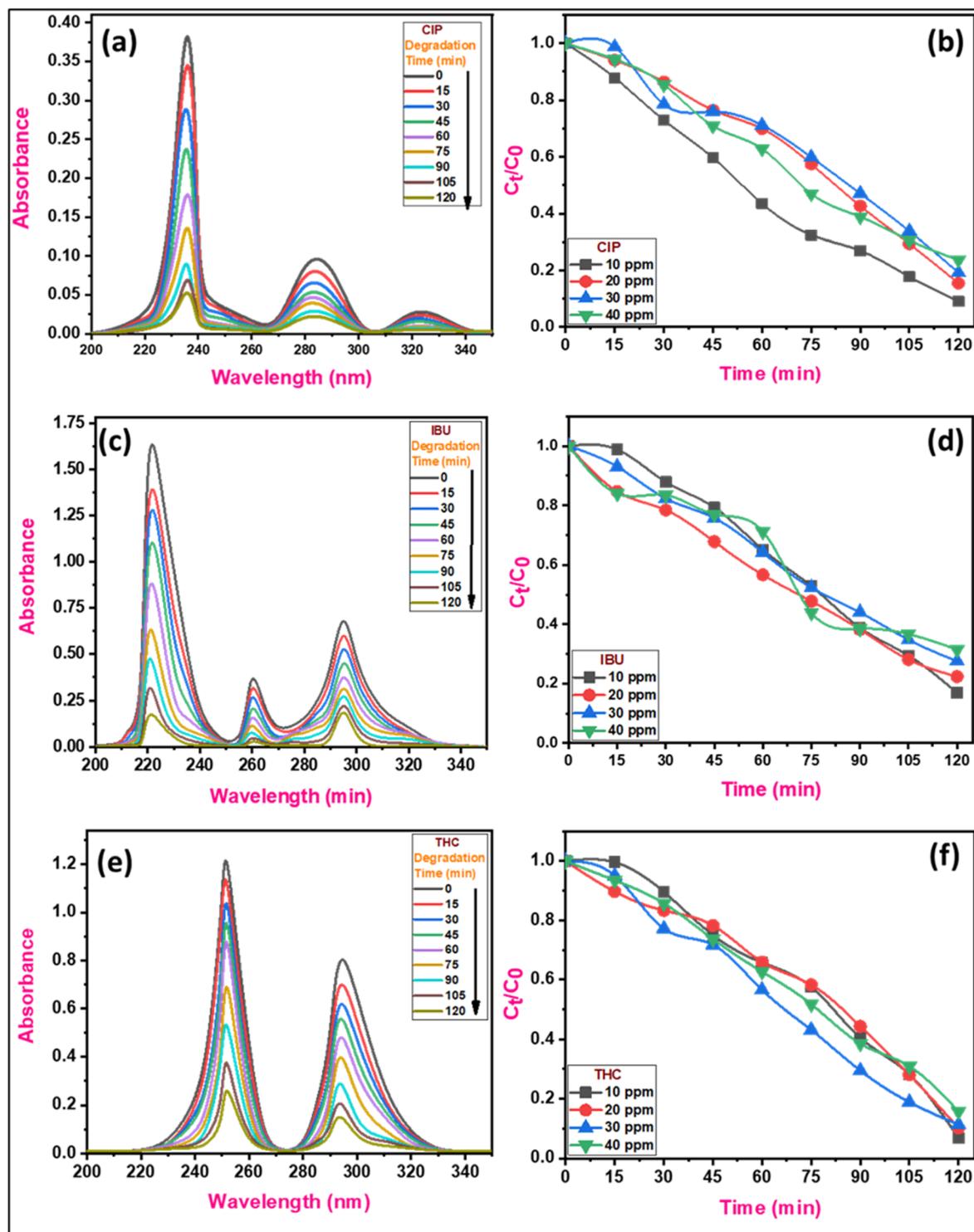
Fig. 7 (a, c, and e) Absorbance spectra of CIP, IBU and THC. (b, d, and f) Photocatalytic degradation of drugs using Fe_3O_4 QDs/rGO NSs under visible irradiation.
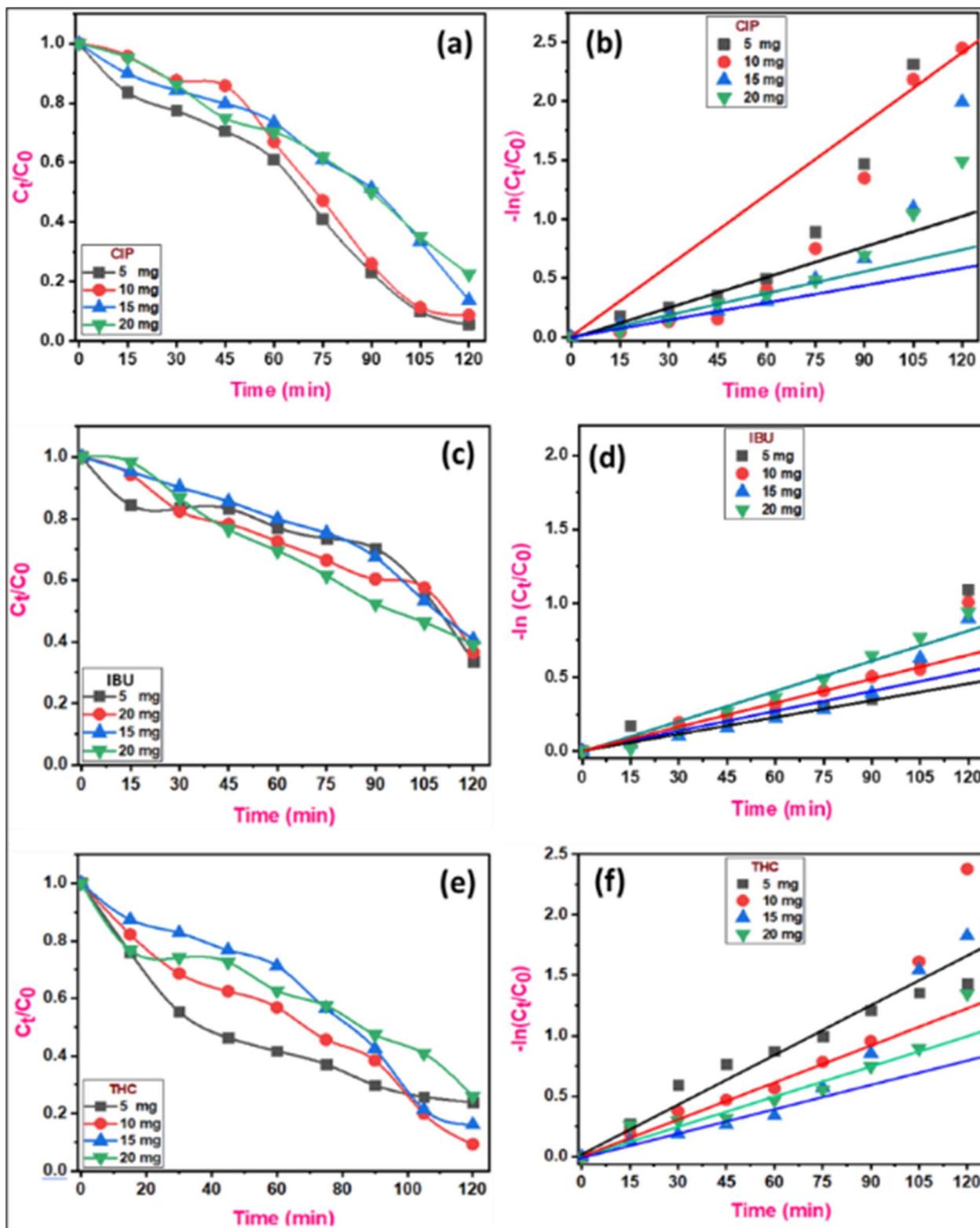
Fig. 8 Effects of Fe$_3$O$_4$ QDs–rGO NSs loading on (a, c, and e) photodegradation, and (b, d, and f) reaction kinetics for CIP, IBU, and THC.

the 10 ppm solution reaching approximately 30% of its initial concentration after 120 minutes. The degradation efficiency diminishes slightly with increasing initial concentration, consistent with active site saturation and lower light penetration at higher pollutant loads.[48]

Further, as shown in Fig. 7(c), the absorbance peaks of IBU, notably around 225 nm and 270 nm, decreased gradually with

illumination time, suggesting successful photocatalytic degradation. Fig. 7(d) shows comparable trends for all concentrations tested, with slightly faster degradation for the 10 and 20 ppm solutions. Notably, degradation of IBU proceeded more linearly compared to CIP, suggesting a potentially different degradation pathway or intermediate formation kinetics.

Fig. 7(e) presents two prominent peaks (∼230 nm and ∼270 nm) for THC that consistently diminish under light irradiation, indicative of effective photodegradation. Fig. 7(f) confirms a significant reduction in C_t/C_0 ratios for all tested

concentrations, with nearly complete degradation ($C_t/C_0 \approx 0.2$) after 120 minutes at 10 ppm. The degradation trend was only mildly affected by concentration, suggesting the strong catalytic activity and high affinity of Fe_3O_4–rGO toward THC. Overall, the Fe_3O_4 QDs–rGO NSs exhibited robust photocatalytic activity toward all tested pharmaceuticals, achieving over 70% degradation in most cases within 2 h. The enhanced performance is attributed to the synergistic effect of Fe_3O_4 QDs and rGO NSs. The Fe_3O_4 provides active sites for hydroxyl radical generation under light, while the rGO facilitates electron transport,
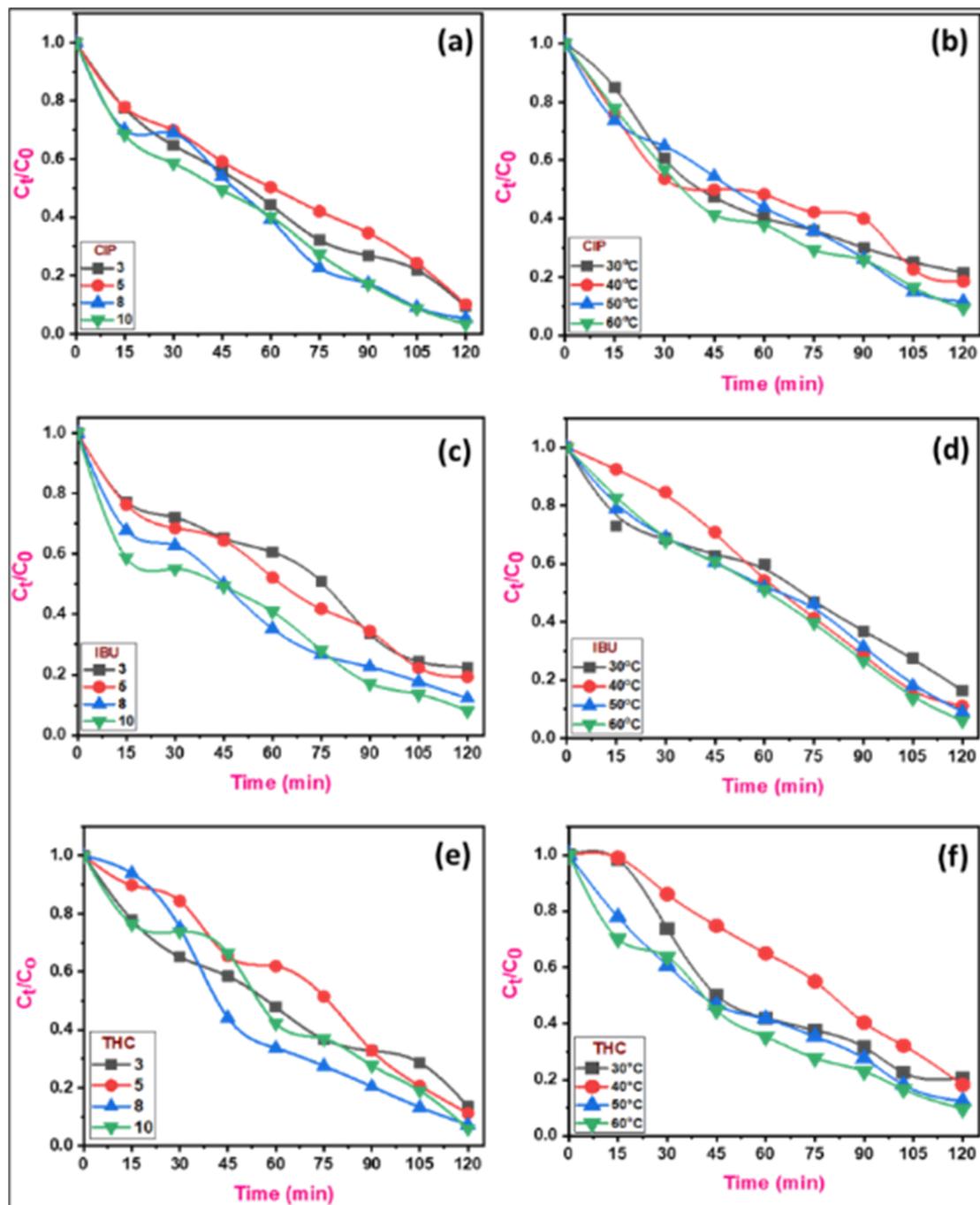

Fig. 9 Effects of (a, c, and e) pH and (b, d, and f) temperature on the photocatalytic degradation of CIP, IBU and THC by Fe_3O_4 QDs/rGO NSs.

suppressing charge recombination and improving photo-catalytic efficiency. The differences in degradation rates among the pollutants can be linked to their molecular structure, light absorption characteristics, and interaction affinity with the NC surface. CIP showed the highest sensitivity to initial concentration, possibly due to its complex aromatic structure and higher molar absorptivity. THC degradation was the most efficient, suggesting favourable adsorption and reactive interactions with the catalyst surface.

3.4. Effect of photocatalyst dose on degradation efficiency

The photocatalytic degradation of CIP, IBU, and THC under UV-visible light using Fe_3O_4 QDs–rGO NSs was systematically evaluated by varying the photocatalyst dosage (5, 10, 15, and 20 mg) while maintaining a fixed pollutant concentration of 10 ppm, as optimized in the previous section. The degradation efficiency and kinetics were monitored over 120 minutes of irradiation (Fig. 8). Fig. 8(a, c, and e) show the degradation profiles of CIP, IBU, and THC, respectively, represented as C_t/C_0 versus time, whereas their reaction kinetics are shown in Fig. 8(b, d, and f). For all three pollutants, the degradation rate generally increased with lower photocatalyst dosages, unexpectedly peaking at 5 mg. This can be attributed to better light penetration and reduced particle aggregation at lower catalyst loads, which facilitate more efficient generation of reactive species such as $\cdot OH$ and $\cdot O_2^-$. At higher dosages, a slight decline in performance was observed, likely due to excessive turbidity and shadowing effects that reduce photon absorption efficiency.[49,50]

3.5. Effect of pH and temperature on degradation efficiency

The photocatalytic degradation of CIP, IBU, and THC under UV light using Fe_3O_4 QDs–rGO NSs was systematically evaluated by varying the pH (3, 5, 8, and 10) and temperature (30 °C, 40 °C, 50 °C, and 60 °C), while maintaining a fixed pollutant concentration of 10 ppm and photocatalyst dose of 10 mg, as optimized in the previous section. The degradation efficiency and kinetics were monitored over 120 minutes of irradiation. Fig. 9 illustrates the influence of pH and temperature on the photocatalytic degradation efficiency of the Fe_3O_4 QDs–rGO NSs against three pharmaceutical contaminants, viz CIP, IBU, and THC. Fig. 9(a, c, and e), display the effect of varying pH levels (3, 5, 8, and 10) on the degradation of CIP, IB, and THC, respectively. In each case, the degradation efficiency increases with rising pH, with the most significant removal observed at pH 8 and 10. This enhanced performance under alkaline conditions can be attributed to the increased formation of reactive oxygen species and improved interaction between the catalyst and pollutant molecules, promoting more efficient degradation pathways. Fig. 9(b, d, and f) demonstrate the effect of temperature (30 °C, 40 °C, 50 °C, and 60 °C) on the degradation of the same compounds. The results show a consistent trend of improved degradation efficiency with increasing temperature. The highest degradation rates are observed at 60 °C for all three drugs, likely due to increased molecular motion, enhanced diffusion, and higher collision frequency between the pollutant molecules and the active sites on the Fe_3O_4 QDs–rGO NSs. The combined analysis confirms that both alkaline pH and elevated temperatures significantly enhance the photocatalytic performance of the Fe_3O_4 QDs–rGO NSs.

Fig. 10 presents a comparative analysis of the degradation efficiency of Fe_3O_4 QDs–rGO NSs toward CIP, IBU, and THC at pH 6 and at 60 °C. In Fig. 10(a), the degradation behavior at pH 10 reveals that all three pollutants undergo a steady decline in concentration over time, indicating effective photocatalytic activity under alkaline conditions. The Fe_3O_4 QDs–rGO NSs exhibit slightly superior degradation efficiency for THC, followed by CIP and then IBU. This suggests that the Fe_3O_4 QDs–rGO NSs exhibit stronger interaction and higher affinity towards THC molecules in alkaline media, potentially due to better adsorption and favourable surface charge interactions.
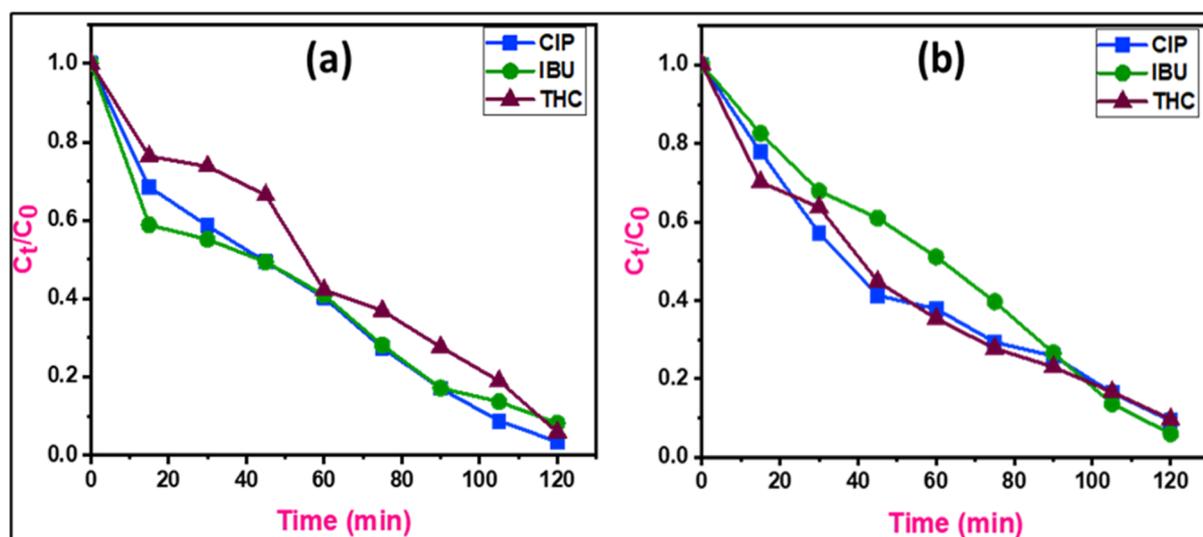

Fig. 10 Comparison of the degradation efficacy of Fe_3O_4 QDs–rGO NSs for CIP, IBU and THC at (a) pH 10 and (b) 60 °C.
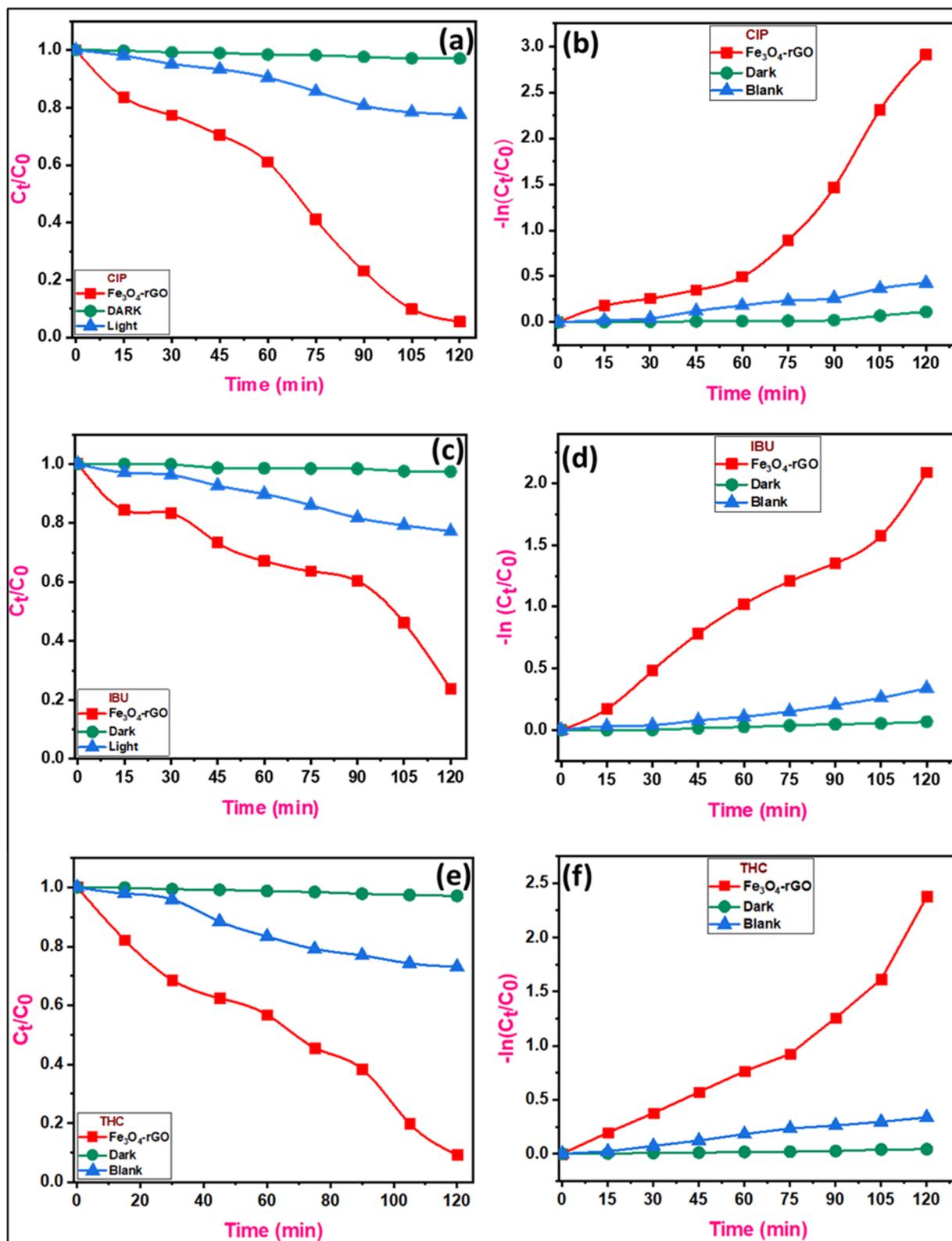
Fig. 11 (a, c, and e) Comparison of Fe_3O_4 QDs/rGO NSs' degradation efficacy and (b, d, and f) reaction kinetics for CIP, IBU and THC.

Fig. 10(b) illustrates the degradation performance at an elevated temperature of 60 °C. Here, an overall enhancement in degradation efficiency is observed for all three drugs, confirming that higher temperatures accelerate photocatalytic reactions by promoting charge carrier mobility and enhancing the generation of reactive oxygen species. Both CIP and THC show nearly similar degradation trends, whereas IBU exhibits slightly lower efficiency throughout the reaction period.

3.6. Degradation performance and kinetics of Fe_3O_4 QDs–rGO NSs

A comparison of the photocatalytic degradation efficiency and corresponding kinetic profiles of Fe_3O_4 QDs–rGO NSs is shown in Fig. 11. Fig. 11(a, c, and e) demonstrate the degradation behavior over 120 minutes under three different conditions: in the presence of Fe_3O_4 QDs–rGO NSs, under dark conditions, and under visible light without the catalyst (blank). The significant reduction in C_t/C_0 values in the presence of the Fe_3O_4 QDs–rGO NSs, compared to the negligible changes under dark and blank conditions, clearly indicates that the photocatalytic activity of the NC plays a major role in degrading the pollutants. For all three pollutants, the degradation rate is most pronounced when the Fe_3O_4 QDs–rGO NSs are employed under illumination, confirming that the material is an effective photocatalyst. Fig. 11(b, d, and f) show the corresponding reaction kinetics expressed as $-\ln(C_t/C_0)$ over time for CIP, IBU, and THC, respectively. The linear increase in $-\ln(C_t/C_0)$ values for the Fe_3O_4 QDs–rGO NSs highlights a pseudo-first-order kinetic behavior for all three drugs, which is typical of photocatalytic degradation processes. The negligible kinetic response observed under dark and blank conditions further confirms that the degradation is primarily due to the photocatalytic activity of the Fe_3O_4 QDs–rGO NSs rather than photolysis alone.

3.7. Kinetic analysis

The photodegradation kinetics were analyzed using the pseudo-first-order model:

$$-\ln(C_t/C_0) = kt$$

where k is the rate constant (min^{-1}), C_0 is the initial concentration, and C_t is the concentration at time t. The linearized plots in Fig. 8b, d, and f confirm pseudo-first-order behavior, with good linearity for all pollutants across the tested dosages.[51–53] The calculated first-order rate constants and the maximum degradation at 120 min are provided in Table 1.

Among the various dosages, 5 mg Fe_3O_4 QDs–rGO NSs yielded the highest degradation rate constants. The higher rate constant and degradation efficiency for CIP suggest that the molecular structure and functional groups of CIP are more susceptible to photocatalytic attack than those of IBU and THC. The efficiency order for degradation was: CIP > THC > IBU.

3.8. Mechanistic implications

The adsorption of antibiotics onto the catalyst surface is a vital preliminary step that strongly influences the overall photocatalytic efficiency. The Fe_3O_4 QDs–rGO NSs exhibit a high BET surface area (168 $m^2\ g^{-1}$) and mesoporous nature (average pore size ≈ 14 nm), providing abundant adsorption sites for antibiotic molecules. The π–π interactions between the aromatic rings of the antibiotic molecules and the π-conjugated graphene surface, along with hydrogen bonding and electrostatic attraction between the surface oxygenated groups (–OH, –COOH, –C=O) of the Fe_3O_4 QDs–rGO NSs and the polar functional groups of the drugs, facilitate strong adsorption. This pre-adsorption effectively increases the local concentration of pollutants around photoactive sites and enhances their activation under visible-light irradiation. The synergistic combination of high surface area, mesoporosity, and surface functionalities of the Fe_3O_4 QDs–rGO NSs thus plays a decisive role in boosting both adsorption and photocatalytic degradation efficiency. The superior photocatalytic activity of the Fe_3O_4 QDs–rGO NSs can be attributed to the synergistic effect between the magnetic Fe_3O_4 QDs and the conductive rGO NSs. Fe_3O_4 facilitates light absorption and reactive radical formation, while rGO suppresses electron–hole recombination by acting as an electron shuttle. This synergy leads to enhanced charge carrier lifetime and improved pollutant degradation efficiency. At optimal conditions (10 mg catalyst dose), the photocatalytic system demonstrated a balance between adequate active site availability and minimized aggregation/shielding effects. Thus, this dose was selected for subsequent optimization studies on pH and temperature. During the photocatalytic degradation process, the key reactive species involved are hydroxyl radicals ($^\bullet OH$) and superoxide radicals ($^\bullet O_2^-$). Upon visible-light irradiation, Fe_3O_4 QDs absorb photons, leading to the excitation of electrons from the valence band (VB) to the conduction band (CB), leaving behind photogenerated holes (h^+). The photogenerated electrons rapidly transfer from Fe_3O_4 to the rGO surface, which acts as an electron mediator to suppress electron–hole recombination. These electrons react with molecular oxygen adsorbed on the catalyst surface to produce $^\bullet O_2^-$ radicals, while the holes oxidize water molecules or surface hydroxyl groups to yield $^\bullet OH$ radicals. Both radicals are highly reactive oxidants that attack the antibiotic molecules, leading to their successive degradation into smaller intermediates
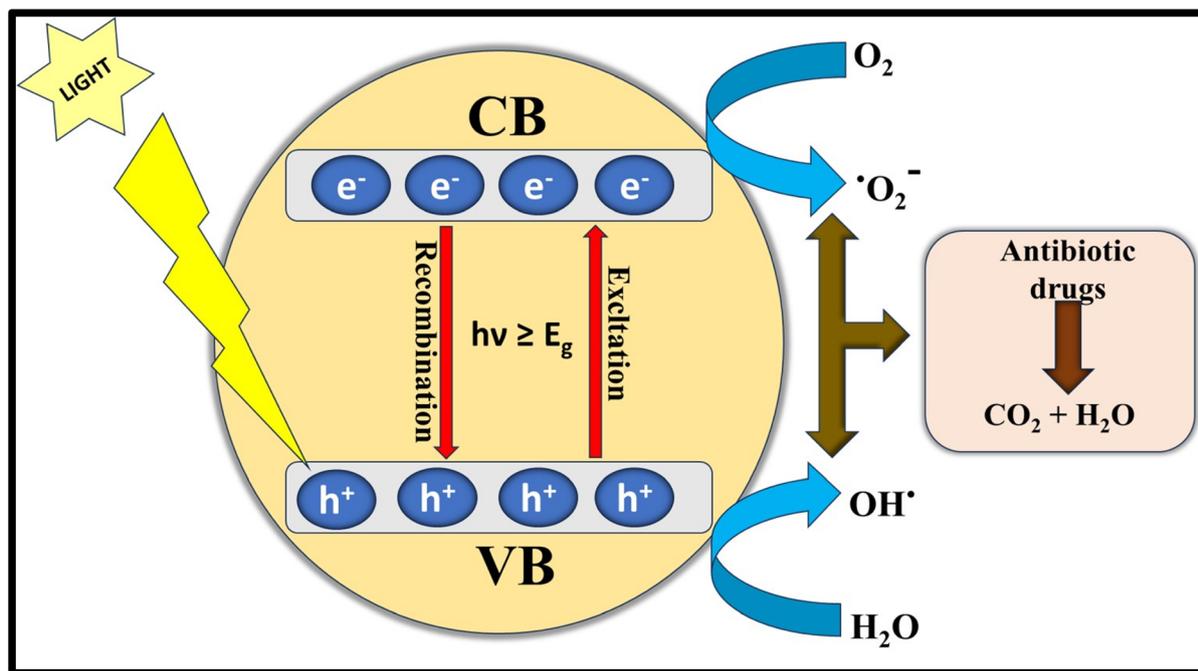
Table 1 Degradation efficiencies, rate constants and R^2 of drugs over Fe_3O_4 QDs–rGO NSs (5 mg)

Drug	% Degradation @120 min	Rate constant (k) (min^{-1})	R^2
CIP	94.53	0.024	0.978
IBU	76.23	0.017	0.928
THC	90.71	0.012	0.981
In dark			
CIP	2.93	0.0009	0.987
IBU	2.56	0.0006	0.921
THC	2.87	0.0004	0.989
Blank			
CIP	22.35	0.0036	0.976
IBU	22.83	0.0028	0.988
THC	26.89	0.0028	0.966

Fig. 12 Proposed mechanism and charge transfer pathway of Fe_3O_4 QDs–rGO NSs under visible-light irradiation.

and eventual mineralization. The synergistic interaction between Fe_3O_4 QDs and the conductive rGO matrix enhances charge separation and increases the generation rate of these active radicals, resulting in improved photocatalytic performance under visible-light irradiation.

The proposed photocatalytic mechanism for the Fe_3O_4 QDs–rGO NSs under visible light is illustrated in Fig. 12. When irradiated with visible light, Fe_3O_4 QDs absorb photons and generate electron–hole pairs. The photogenerated electrons (e^-) in the conduction band of Fe_3O_4 are rapidly transferred to the rGO surface, which serves as an electron-accepting and conducting medium. The accumulated electrons on rGO react with dissolved O_2 to produce superoxide radicals ($^{\bullet}O_2^-$), while the holes (h^+) in the valence band of Fe_3O_4 oxidize surface hydroxyl groups or H_2O molecules to form hydroxyl radicals ($^{\bullet}OH$). These highly reactive species attack and degrade antibiotic molecules into smaller, non-toxic intermediates. The intimate Fe–O–C interfacial bonding and conductive network of rGO facilitate efficient charge separation, thereby minimizing recombination and enhancing the overall photocatalytic efficiency.

As shown in Table 1, the present Fe_3O_4 QDs–rGO NSs achieve 94.5% CIP degradation within 120 min under visible-light irradiation (400–750 nm, 400-W tungsten lamp) using only 0.10 g L^{-1} of catalyst. The corresponding apparent rate constant ($k = 0.024$ min^{-1}) is comparable to or higher than many previously reported Fe_3O_4-based systems that often require higher catalyst loadings and longer irradiation times. In addition, our material offers the advantages of a one-step green synthesis and excellent reusability over five cycles. A comparison of the performance of the bioinspired Fe_3O_4 QDs–rGO NSs with several recently reported Fe_3O_4 and rGO-based photocatalysts is shown in Table 2. This comparison highlights that the Fe_3O_4 QDs–rGO NSs prepared *via* the *Thuja occidentalis* leaf extract-mediated route combine high photocatalytic efficiency with sustainability and operational simplicity, confirming the advancement achieved over existing Fe_3O_4/rGO-based catalysts.

Table 2 Comparative performance analysis of the bioinspired Fe_3O_4 QDs–rGO NSs with several recently reported Fe_3O_4 and rGO-based photocatalysts

| Sr. no.	Catalyst	Target pollutant	Light source (range/type)	Reaction time	Degradation (%)	References
1	Fe_3O_4/CuO on carbon	CIP	Visible light (halogen/visible)	120 min	98.5	54
2	MoS_2@Fe_3O_4 (photo-Fenton)	THC	Visible light (photo-Fenton conditions; H_2O_2-assisted)	60 min	98.6	55
3	Fe_3O_4/Bi_2WO_6 heterojunction	CIP	Visible light	15 min	~99.7	56
4	Ternary Fe_3O_4/g-C_3N_4/rGO	THC	Visible light	60 min	86.7	57
5	$CuFe_2O_4$/rGO/halloysite	CIP	Visible light	~60 min	99	58
6	Fe_3O_4 QDs–rGO NSs	CIP	400–750 nm (400 W tungsten lamp), ~120 mW cm^{-2}	120 min	94.5	Present work
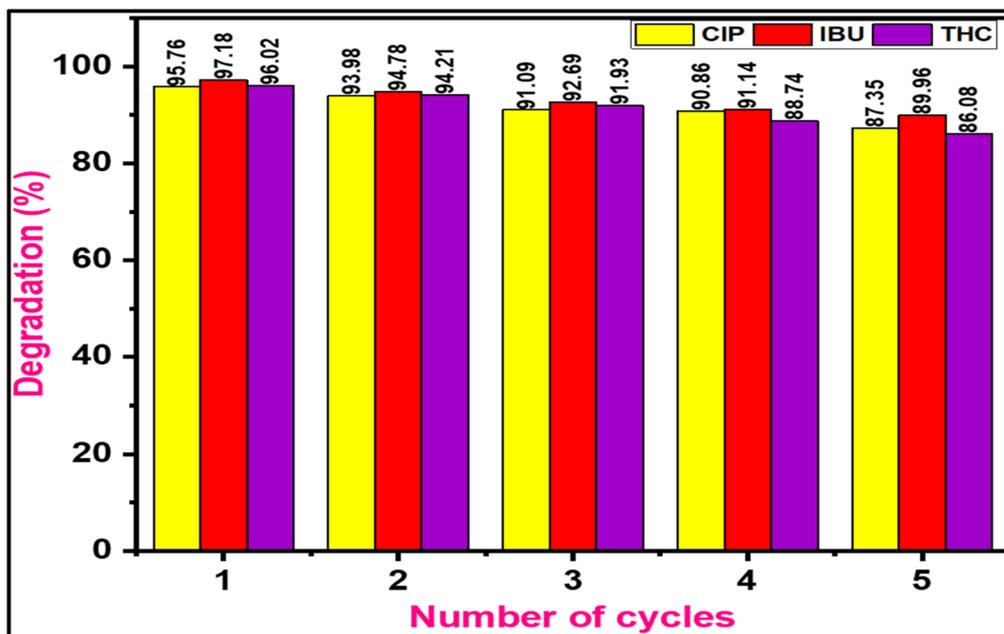
Fig. 13 Reusability of Fe$_3$O$_4$ QDs–rGO NSs against CIP, IBU, and THC as indicated.

3.9. Reusability

The removal efficiency and reusability of NCs are critical for their practical application in industrial settings. To evaluate these aspects, recyclability experiments were conducted by recovering the photocatalyst after each cycle, washing it with distilled water, drying it, and reusing it for the subsequent cycle over five consecutive cycles. The outcomes of these tests are illustrated in Fig. 13. The reusability tests presented in Fig. 13 evaluate the Fe$_3$O$_4$ QDs–rGO NSs over five successive cycles for the degradation of three pharmaceutical contaminants: CIP, IBU, and THC. Each test was conducted using a constant catalyst dose of 10 mg and a drug concentration of 10 ppm. In the case of CIP degradation (Fig. 13), the photocatalytic performance shows a slight decrease from the first to the fifth cycle, indicating good recyclability. The degradation efficiency remains high, with only a minor drop in activity, suggesting that the Fe$_3$O$_4$ QDs–rGO NSs maintain their structural integrity and active sites during repeated use. For IBU degradation (Fig. 13), the initial degradation efficiency starts at 97.18% and gradually decreases to 89.66% by the fifth cycle. Although the degradation percentage declines, the photocatalyst still retains over 89% of its efficiency, demonstrating excellent reusability and photocatalytic resilience in successive applications. In the case of THC degradation (Fig. 13), the trend is similar, with a slight but progressive decrease in performance over the five cycles. Despite this reduction, the Fe$_3$O$_4$ QDs–rGO NSs still show significant degradation ability, highlighting their potential for repeated applications in environmental remediation.

4. Conclusion

Fe$_3$O$_4$ QDs on rGO NSs were successfully biosynthesized *via* a one-step hydrothermal method using *Thuja occidentalis* leaf extract.

Characterization through various analytical and spectroscopic techniques confirmed the formation of well-dispersed nearly homogeneous Fe$_3$O$_4$ QDs ($\sim$7 $\pm$ 2 nm) anchored on the reduced graphene oxide (rGO) sheets. Moreover, the biosynthesized NC demonstrated high surface area (168 m^2 g^{-1}), mesoporous nature, and strong Fe$_3$O$_4$–rGO interaction. The photocatalytic performance of the Fe$_3$O$_4$ QDs–rGO NSs was evaluated against CIP, IBU, and THC, and the material exhibited superior degradation efficiency toward CIP, achieving $\sim$94.53% removal efficiency at 5 mg L^{-1} within 120 minutes under visible irradiation. In contrast, IBU and THC showed lower degradation efficiencies ($\sim$76.23% and $\sim$90.71%, respectively). However, THC demonstrated improved performance ($\sim$90.71%) at higher concentrations (10 mg L^{-1}). Optimal photocatalytic activity was observed under neutral pH and elevated temperatures, particularly for CIP. Kinetic analysis using the Langmuir–Hinshelwood model indicated that the degradation followed pseudo-first-order kinetics. Importantly, the Fe$_3$O$_4$ QDs–rGO NSs demonstrated excellent reusability, maintaining high removal efficiency over five cycles. These findings underscore the potential of bioinspired Fe$_3$O$_4$ QDs–rGO NSs as an efficient, sustainable material for futuristic application such as environmental remediation, particularly in wastewater treatment, photocatalytic degradation, adsorption, and the purification of pharmaceutical-contaminated water sources.

Author contributions

Conceptualization: Ajay Potbhare, Rohit Madankar, Pavan Bhilkar, Ahmed Abdala and Ratiram Chaudhary; visualization: Ajay Potbhare, Rohit Madankar, Shubham Tripathy, Aniket Kahate; supervision: Subhash Somkuwar, Ahmed Abdala and Ratiram Chaudhary; writing – original draft: Ajay Potbhare, Rohit Madankar, and Ratiram Chaudhary; writing, reviewing &

editing: Rameshwar Adhikari, Leonard Ng Wei Tat, Ahmed Abdala and Ratiram Chaudhary.

Data availability

All data that support the findings of this study are included in the article.

Conflicts of interest

The authors declare no conflict of interest, financial or otherwise.

Acknowledgements

References

1 S. Dutta, S. Adhikary, S. Bhattacharya, D. Roy, S. Chatterjee, A. Chakraborty, D. Banerjee, A. Ganguly, S. Nanda and P. Rajak, *J. Environ. Manage.*, 2024, **353**, 120103.

2 A. O. C. Iroegbu, S. S. Ray, V. Mbarane, J. C. Bordado and J. P. Sardinha, *ACS Omega*, 2021, **6**, 19343–19355.

3 M. Rajabi, S. Keihankhadiv, Suhas, I. Tyagi, R. R. Karri, M. Chaudhary, N. M. Mubarak, S. Chaudhary, P. Kumar and P. Singh, *J. Nanostruct. Chem.*, 2023, **13**, 43–65.

4 P. Zhang, M. Yang, J. Lan, Y. Huang, J. Zhang, S. Huang, Y. Yang and J. Ru, *Toxics*, 2023, **11**, 828.

5 N. Saxena, M. M. Islam, S. Baliyan and D. Sharma, *RSC Sustainability*, 2023, **1**, 2148–2161.

6 C. M. Costa, V. F. Cardoso, P. Martins, D. M. Correia, R. Gonçalves, P. Costa, V. Correia, C. Ribeiro, M. M. Fernandes, P. M. Martins and S. Lanceros-Méndez, *Chem. Rev.*, 2023, **123**, 11392–11487.

7 R. Mukhopadhyay, B. Sarkar, E. Khan, D. S. Alessi, J. K. Biswas, K. M. Manjaiah, M. Eguchi, K. C. Wu, Y. Yamauchi and Y. S. Ok, *Crit. Rev. Environ. Sci. Technol.*, 2022, **52**, 2611–2660.

8 A. Roy, A. Sharma, S. Yadav, L. T. Jule and R. Krishnaraj, *Bioinorg. Chem. Appl.*, 2021, **2021**, 1764647.

9 S. Dutta, A. Sinelshchikova, J. Andreo and S. Wuttke, *Nanoscale Horiz.*, 2024, **9**, 885–899.

10 O. Zaytseva and G. Neumann, *Chem. Biol. Technol. Agric.*, 2016, **3**, 1–26.

11 L. Ma, M. Zhou, C. He, S. Li, X. Fan, C. Nie, H. Luo, L. Qiu and C. Cheng, *Green Chem.*, 2019, **21**, 4887–4918.

12 B. Anegbe, I. H. Ifijen, M. Maliki, I. E. Uwidia and A. I. Aigbodion, *Environ. Sci. Eur.*, 2024, **36**, 15.

13 K. M. Cho, K. H. Kim, H. O. Choi and H. T. Jung, *Green Chem.*, 2015, **17**, 3972–3978.

14 Z. Yang, S. Zhou, X. Feng, N. Wang, O. Ola and Y. Zhu, *Nanomaterials*, 2023, **13**, 2028.

15 R. Madankar, M. Umekar, G. Bhusari, A. Mondal, M. Raish, M. Afzal, M. Norek and R. Chaudhary, *Sci. Rep.*, 2025, **15**, 28999.

16 A. K. Potbhare, R. S. Madankar, S. S. Tripathy, A. Mondal, A. S. Kahate, P. Bhilkar, M. Norek, M. F. Desimone and R. G. Chaudhary, *Nanoscale*, 2025, **17**, 24072–24087.

17 R. K. Upadhyay, N. Soin and S. S. Roy, *RSC Adv.*, 2014, **4**, 3823–3851.

18 A. B. Ponnusami, S. Sinha, H. Ashokan, M. V. Paul, S. P. Hariharan, J. Arun, K. P. Gopinath, Q. H. Le and A. Pugazhendhi, *Environ. Res.*, 2023, **237**, 116944.

19 C. Agarwal and A. K. Pandey, *Environ. Sci.: Adv.*, 2023, **2**, 1306–1339.

20 G. Ren, H. Han, Y. Wang, S. Liu, J. Zhao, X. Meng and Z. Li, *Nanomaterials*, 2021, **11**, 1804.

21 Y. J. Yuan, Y. Yang, Z. Li, D. Chen, S. Wu, G. Fang, W. Bai, M. Ding, L. X. Yang, D. P. Cao and Z. T. Yu, *ACS Appl. Energy Mater.*, 2018, **1**, 1400–1407.

22 R. G. Chaudhary, V. Sonkusare, G. Bhusari, A. Mondal, A. Potbhare, H. Juneja, A. Abdala and R. Sharma, *Environ. Res.*, 2023, **222**, 115363.

23 A. K. Potbhare, S. K. Tarik Aziz, M. Monis Ayyub, A. Kahate, R. Madankar, S. Wankar, A. Dutta, A. Abdala, S. H. Mahmood, R. Adhikari and R. G. Chaudhary, *Nanoscale Adv.*, 2024, **6**, 2539–2568.

24 M. H. Kahsay, N. Belachew, A. Tadesse and K. Basavaiah, *RSC Adv.*, 2020, **10**, 34916–34927.

25 T. Govindasamy, N. K. Mathew and B. Subramanian, *Energy Fuels*, 2024, **38**, 21144–21161.

26 J. Scaria and P. V. Nidheesh, *Environ. Sci.: Water Res. Technol.*, 2022, **8**, 1261–1276.

27 M. Moztahida, M. Nawaz, J. Kim, A. Shahzad, S. Kim, J. Jang and D. S. Lee, *Chem. Eng. J.*, 2019, **370**, 855–865.

28 M. Maruthupandy, D. Riquelme, G. Rajivgandhi, T. Muneeswaran, W. S. Cho, M. Anand, N. Manoharan and F. Quero, *J. Environ. Chem. Eng.*, 2021, **9**, 106014.

29 P. P. Singh, G. Pandey, Y. Murti, J. Gairola, S. Mahajan, H. Kandhari, S. Tivari and V. Srivastava, *RSC Adv.*, 2024, **14**, 20492–20515.

30 R. Wu, Y. Wang, J. Wang, G. Tian, Y. Li and C. Liu, *RSC Adv.*, 2025, **15**, 27128–27138.

31 A. Kaur, S. Kumar, H. Kaur, G. S. Lotey, P. P. Singh, G. Singh, S. Kumar, J. Dalal, G. Bouzid, M. Misra and R. Pandey, *Mater. Adv.*, 2024, **5**, 8111–8131.

32 I. Ahmad, M. S. Athar, M. Muneer, H. M. Altass, R. Felemban and S. A. Ahmed, *Nanoscale*, 2025, **17**, 3822–3836.

33 L. Yin, K. Wang, L. Jiang, Y. Xi, Z. Xu, Z. Song and H. Zhou, *RSC Adv.*, 2025, **15**, 16337–16347.

34 A. K. Potbhare, R. G. Chaudhary, P. B. Chouke, S. Yerpude, A. Mondal, V. N. Sonkusare, A. R. Rai and H. D. Juneja, *Mater. Sci. Eng. C.*, 2019, **99**, 783–793.

35 X. Chen, Z. Qu, Z. Liu and G. Ren, *ACS Omega*, 2022, **7**, 23503–23510.

36 W. S. Hummers Jr and R. E. Offeman, *J. Am. Chem. Soc.*, 1958, **80**, 1339.

37 D. K. Padhi, T. K. Panigrahi, K. Parida, S. K. Singh and D. P. Mishra, *ACS Sustain. Chem. Eng.*, 2017, **5**, 10551–10562.

38 A. Bergmann, E. Martinez-Moreno, D. Teschner, P. Chernev, M. Gliech, J. F. De Araújo, T. Reier, H. Dau and P. Strasser, *Nat. Commun.*, 2015, **6**, 8625.

39 P. M. Mishra, G. K. Naik, A. Nayak and K. M. Parida, *Chem. Eng. J.*, 2016, **299**, 227–235.

40 C. Y. San and M. M. Don, *J. Phys. Sci.*, 2013, **24**, 83–96.

41 S. Dutta, A. Madhuri, S. Jena, S. Laha and B. P. Swain, *Appl. Phys. A*, 2024, **130**, 719.

42 G. Xie, P. Xi, H. Liu, F. Chen, L. Huang, Y. Shi, F. Hou, Z. Zeng, C. Shao and J. Wang, *J. Mater. Chem.*, 2012, **22**, 1033–1039.

43 S. Liu, T. H. Zeng, M. Hofmann, E. Burcombe, J. Wei, R. Jiang, J. Kong and Y. Chen, *ACS Nano*, 2011, **5**, 6971–6980.

44 T. Ramanathan, A. A. Abdala, S. Stankovich, D. A. Dikin, M. Herrera-Alonso, R. D. Piner, D. H. Adamson, H. C. Schniepp, X. R. R. S. Chen, R. S. Ruoff and S. T. Nguyen, *Nat. Nanotechnol.*, 2008, **3**, 327–331.

45 K. A. Mkhoyan, A. W. Contryman, J. Silcox, D. A. Stewart, G. Eda, C. Mattevi, S. Miller and M. Chhowalla, *Nano Lett.*, 2009, **9**, 1058–1063.

46 D. K. Padhi, T. K. Panigrahi, K. Parida, S. K. Singh and D. P. Mishra, *ACS Sustain. Chem. Eng.*, 2017, **5**, 10551–10562.

47 L. Shen, L. Huang, S. Liang, R. Liang, N. Qin and L. Wu, *RSC Adv.*, 2014, **4**, 2546–2549.

48 V. N. Sonkusare, R. G. Chaudhary, G. S. Bhusari, A. Mondal, A. K. Potbhare, R. K. Mishra, H. D. Juneja and A. A. Abdala, *ACS Omega*, 2020, **5**, 7823–7835.

49 D. P. Singh, C. E. Herrera, B. Singh, S. Singh, R. K. Singh and R. Kumar, *Mater. Sci. Eng. C*, 2018, **86**, 173–197.

50 P. B. Chouke, K. M. Dadure, A. K. Potbhare, G. S. Bhusari, A. Mondal, K. Chaudhary, V. Singh, M. F. Desimone, R. G. Chaudhary and D. T. Masram, *ACS Omega*, 2022, **7**, 20983–22099.

51 M. Yusuf, M. Kumar, M. A. Khan, M. Sillanpää and H. Arafat, *Adv. Colloid Interface Sci.*, 2019, **273**, 102036.

52 S. T. Aziz, M. Umekar, I. Karajagi, S. K. Riyajuddin, K. V. R. Siddhartha, A. Saini, A. Potbhare, R. G. Chaudhary, V. Vishal, P. C. Ghosh and A. Dutta, *Cell Rep. Phys. Sci.*, 2022, **3**, 101106.

53 R. S. Madankar, P. Bhilkar, M. Raish, A. Potbhare, M. Norek, S. Somkuwar, A. Daddemal-Chaudhary, A. Mondal and R. G. Chaudhary, *Sci. Rep.*, 2025, **15**, 21179.

54 V. A. Tran, T. L. H. Nguyen and V. D. Doan, *Chemosphere*, 2021, **270**, 129417.

55 Z. L. Liu, J. H. Sun, B. Liu, Y. N. Chen and W. Feng, *Water*, 2025, **17**, 235.

56 B. Zhu, D. Song, T. Jia, W. Sun, D. Wang, L. Wang, J. Guo, L. Jin, L. Zhang and H. Tao, *ACS Omega*, 2021, **6**, 1647–1656.

57 J. Shan, X. Wu, C. Li, J. Hu, Z. Zhang, H. Liu, P. Xia and X. Huang, *Environ. Sci. Pollut. Res.*, 2023, **30**, 8098–8109.

58 H. S. Ngo, T. L. Nguyen, N. T. Tran and H. C. Le, *Water*, 2023, **15**, 1569.